applied sciences

MDPI

Article

Morphological Alterations of Granitic Hot Dry Rock (HDR) Due to Short-Term Interactions with Alkaline Salt Solutions and Their Implications on Single-Fracture Permeability

Ou Jiang [1], Dehua Hu [2], Xiuhua Zheng [1,*], Pengxiang Zhang [1], Renjie Zhang [3] and Yousheng Feng [4]

[1] State Key Laboratory of Deep Earth Exploration and Imaging, School of Engineering and Technology, China University of Geosciences (Beijing), Beijing 100083, China; 3002220034@email.cugb.edu.cn (O.J.); 2002240072@email.cugb.edu.cn (P.Z.)
[2] Research Institute of Uranium Geology, China National Nuclear Corporation, Beijing 100822, China; hudehua@briug.cn
[3] Petroleum Engineering Research Institute, PetroChina Dagang Oilfield Company, Tianjin 300280, China; zhang_rj616@163.com
[4] Hebei Weiye Geothermal New Energy Technology Co., Ltd., Handan 057650, China; xiangmubu006@163.com
* Correspondence: xiuhuazh@cugb.edu.cn; Tel.: +86-159-1106-2856

Abstract

Water–rock interaction (WRI) due to fluid invasion into formation fractures causes potential formation damage during drilling in hot dry rock (HDR) reservoirs. Due to the developed artificial fractures, drilling fluids will contact and interact with HDR reservoir fractures, leading to alterations in fracture characteristics. With the increasing popularity of brine-based drilling and completion fluids, these alterations induced by WRI could be further enhanced, which requires investigations. In this study, short-term WRI experiments between the HDR and three reactive solutions, including pure water and alkaline (pH = 10) 6 wt% NaCl/KCl solutions, under temperatures of 25 °C and 180 °C, were carried out. Rock-surface topography alterations were identified using laser scanning. Morphological alteration mechanisms were revealed through microscopic and mineralogical alteration determination using a field emission scanning electronic microscope. Hydrogeochemical simulations, including reaction kinetics and equilibrium, were conducted to support the mineralogical alterations. Implications of morphological alterations on fracture permeability were demonstrated based on a roughness–permeability model. The results show that interactions with the alkaline NaCl solution cause the smoothening of the rock surface due to a coating effect of secondary silicate precipitations, while interactions with pure water and the alkaline KCl solution result in rock-surface roughening because of feldspar dissolution, differential mineral dissolution and biotite hydrolysis dispersion. The secondary precipitations either cover or fill the pores and cracks, the dissolved feldspar enlarges the pores and cracks, the differential mineral dissolution coarsens the rock surfaces, and the biotite hydrolysis dispersion generates pores and cracks on its surfaces. An increase or a decrease in surface roughness induces a corresponding increase or decrease in fracture permeability, because the roughness augmentation (roughening) enlarges seepage channel spaces while roughness reduction (smoothening) narrows them. This work reveals potential formation damage induced by drilling fluid invasion into fractures within HDR geothermal reservoirs, and provides theoretical insights for mitigating such damage.

Keywords: hot dry rock; drilling fluids; water–rock interactions; morphological alterations; fracture permeability

Check for updates

Academic Editor: Kun Sang Lee

Received: 17 July 2026
Revised: 23 August 2026
Accepted: 27 August 2026
Published: 29 August 2026

Copyright: © 2026 by the authors. Licensee MDPI, Basel, Switzerland. This article is an open access article distributed under the terms and conditions of the Creative Commons Attribution (CC BY) license.

1. Introduction

Geothermal energy is a promising renewable energy, which stores within geothermal reservoirs [1,2]. Compared to relatively shallow geothermal reservoirs, deep geothermal reservoirs have a higher temperature and larger reserves [3], indicating a greater exploitation potential. The deep geothermal reservoirs commonly have a poor formation permeability, and an enhanced geothermal system (EGS) is required to enable fluid circulation and heat extraction by creating an artificial fracture network within the reservoirs. Hot dry rock (HDR) is a typical type of deep geothermal reservoirs, where reservoir formations predominantly consist of granite and contain no or little fluids, situated at a depth of 3–10 km with a temperature ranging from 150 to 650 °C [4,5]. An injection well is first drilled into a target HDR reservoir, followed by artificial fracturing of the reservoir formation. Then, a production well is drilled and connected to the fracture network to establish a fluid circulation pathway [4]. However, despite the permeability improvement due to artificial fracturing, the fractures facilitate the loss of drilling and completion (D&C) fluid circulation into the reservoir production zone [6–8]. This leads to damage to formation permeability through the interactions between the fluids and rocks, potentially increasing exploitation risks and reducing reservoir productivity [9–11].

A series of water–rock interaction (WRI) mechanisms can result in reservoir damages, including the hydration, shrinkage, hydrolysis, dissolution and precipitation of minerals and fines migration [12–14]. The main reason is the fracture-aperture alteration resulting from these WRI mechanisms [15,16], which is primarily attributed to the changes in rock–surface morphology. For example, the two sides of a rock fracture become unmated due to mineral dissolution, thereby increasing the effective fracture aperture and permeability [17]. Various degrees of mineral dissolution enhance the discreteness of the height and the deviation degree of the datum plane on rock surfaces, which causes an increase in the rock-surface roughness [18]. This is because the heterogeneity of reactive minerals and their nonuniform distribution result in a nonuniform mineral alterations on rock surfaces [16]. The influencing degree is related to rock types and their compositions, flow rates (i.e., Reynolds numbers of the fluid flow), and temperatures, as well as the chemical contents of the fluids [16,18–20]. As a type of reactive fluids, the invasion of D&C fluids into reservoir formations and their interactions with the rock can readily induce a variety of damages [21]. D&C fluid invasion results in the dissolution of the micro-asperities on the fracture surfaces, inducing slip displacement and further aggravating formation stress sensitivity [22].

Currently, brine-based D&C fluids manifest their significance in replacing oil-based and conventional water-based D&C fluids. Taking brine as the base solution for preparing D&C fluids is not only in accordance with the local water resource conditions, but also achieves the required performance of D&C fluids, including rheological, filtration reduction, anti-swelling, and corrosion inhibition properties [23–25]. Salt content in brine-based D&C fluids functions as an activity regulator, preventing water molecules from entering the reservoir formations [26]. During the drilling of well GPK2 at the European HDR site, brine-based drilling fluids were also utilized, aiming at balancing the formation pressure [27]. Qinghai Province is located in the northwest of China, where surface fresh water resources are scarce and saline–alkali land is widespread [28]. The Gonghe Basin in Qinghai Province is a typical HDR site in China [29], and the geothermal water there is alkaline with a high salinity [30]. Using brine-based drilling fluids is an applicable and economic method for drilling HDR reservoirs in the Gonghe Basin. However, alkaline salt solutions enhance the reactivity of drilling fluids, leading to more active WRI [10]. This intensifies the changes in fracture permeability caused by morphological alterations on rock-fracture surfaces resulting from WRI.

To address the above issue, in this paper, the morphological alterations of granitic hot dry rock (HDR) due to short-term interactions with alkaline salt solutions and their implications on single-fracture permeability were investigated. Firstly, referring to the brine-based drilling fluid applied in the HDR project of Soultz, France [27], short-term WRI experiments, between HDR and alkaline sodium chloride (NaCl) and potassium chloride (KCl) solutions, were carried out. Subsequently, the morphological alterations on rock surfaces due to WRI and their mechanisms were determined, including surface topography, along with microscopic and mineralogical alterations. Hydrogeochemical simulations were conducted to support the mineralogical alterations. Finally, based on a roughness–permeability model, the implication of morphological alterations on single-fracture permeability was revealed.

2. Materials and Methods

2.1. Materials

The granitic HDR rock sample was recovered from a geothermal well at a depth of 2350 m, in the Gonghe Basin, Qinghai Province, as seen in Figure 1. The alkaline salt solutions include alkaline sodium chloride (NaCl) and alkaline potassium chloride (KCl) solutions. A pure water group is used as the control. As reported by [30], the main cations in the geothermal water of Gonghe Basin are Na^+ + K^+, and the dominant anion is Cl^-. Additionally, NaCl and KCl are commonly used inorganic salts in brine-based drilling fluids [26,31]. Drilling fluids with a salt content exceeding 1 wt% are referred to as brine-based drilling fluids [31]. Further, according to [27], the salt content herein is 6 wt%. The alkalinity of the salt solutions was achieved by adding hydroxides that contain the same cation as the corresponding salts, and the solution pH value was adjusted to 10 [10,31]. Details of the utilized chemicals are given in Table 1.

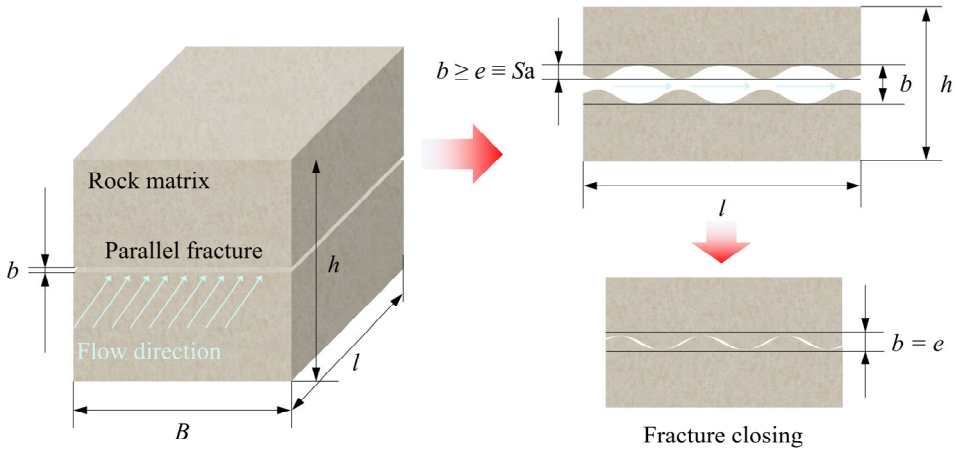


Figure 1. Schematic diagram of the rough parallel fracture model.

Table 1. Details of the utilized chemicals.

Chemicals	Functions	Concentrations (%)	Providers
NaCl	Density regulator	99.5	Sinopharm Chemical Reagent Co., Ltd., Beijing, China
KCl	Density regulator	99.5	Shanghai Aladdin Co., Ltd., Shanghai, China
NaOH	pH regulator	96	Shanghai Aladdin Co., Ltd., Shanghai, China
KOH	pH regulator	85	Shanghai Aladdin Co., Ltd., Shanghai, China

2.2. Experiments and Tests

2.2.1. Mineral Characterization and Rock Sample Preparation

WRI is influenced by mineral characteristics, and hence the contents, grain dimension and specific surface area of the HDR minerals were determined [12,15,17]. The mineral contents were determined by X-ray diffraction (XRD) using the D/Max-RC type diffractometer from Rigaku Co., Ltd., Tokyo, Japan. The rock sample was ground into powders with a size smaller than 300 mesh for XRD tests. The grain dimension of minerals was identified by observing the thin sections of the rock sample using a BX51 polarizing microscope from Olympus Co., Ltd., Tokyo, Japan. The specific surface area of minerals was obtained from [12,15] based on grain dimension. For WRI experiments, the rock sample was made into cubes with a size of 10 mm × 10 mm × 10 mm, with one side being polished for the morphological observations. The cubes (mainly the polished sides) were cleaned uniformly at a constant rate with deionized water. During cleaning, the electrical conductivity of washed deionized water was measured repeatedly using a conductivity meter until the measured value was close to the electrical conductivity of original deionized water and remained relatively stable. This cleaning protocol ensures the removal of exterior species from rock surfaces before WRI, and eliminates residual solutes from the rock surfaces after WRI. After cleaning, the rock samples were dried in a drying oven at 105 °C for 24 h. The drying conditions can prevent any mineralogical or micro-structural alterations to the granite rock samples [10]. Six cleaned cubic rock samples were prepared for WRI experiments numbered 1 to 6, namely, #1–#6. Each sample underwent identical experimental and testing procedures under various conditions, followed by observation of original rock-surface morphology and mineralogy, and the subsequent WRI experiments, as well as observation of rock-surface morphology and mineralogy after WRI experiments.

2.2.2. Solution Preparation

Firstly, 6 wt% salt was thoroughly mixed with pure water in a glass beaker. Then, the hydroxides were added into the salt solutions until the pH values reached around 10. The pH values of the solutions were obtained using a digital pH meter. After mixing, the solutions were heated to boiling and kept boiling for 10 min to remove dissolved gases [10]. The density of the solutions (ρ_{sol}) was identified using a digital liquid densitometer. The initial element content concentrations of the prepared solutions were also determined by the Inductively Coupled Plasma Optical Emission Spectrometer (ICP-OES) 725 ES from Agilent Technologies Co., Ltd., Santa Clara, CA, USA, including silicon (Si), aluminum (Al), sodium (Na), potassium (K), iron (Fe), calcium (Ca), and magnesium (Mg). The detection limits of Si, Al, Na, K, Fe, Ca, and Mg are 2.5 μg/L, 0.9 μg/L, 2 μg/L, 4 μg/L, 0.8 μg/L, 0.06 μg/L and 0.04 μg/L, respectively. Pure water, alkaline NaCl solution and alkaline KCl solution were utilized in #1/#4, #2/#5, and #3/#6, respectively. Details of the prepared solutions are provided in Table 2.

Table 2. Details of the prepared solutions.

No.	Formulas	ρ_{sol} (g/cm^3)	pH	Element Content Concentrations (mg/L)						
				Si	Al	Na	K	Fe	Ca	Mg
#1/#4	Water	1.00	8.04	8.913×10^{-1}	2.890×10^{-2}	1.873×10^{1}	3.475	4.090×10^{-2}	4.020×10^{1}	1.517×10^{1}
#2/#5	Water + 6 wt% NaCl + NaOH	1.06	9.89	7.463×10^{-1}	3.220×10^{-2}	2.595×10^{4}	1.667×10^{1}	7.300×10^{-3}	3.887×10^{1}	8.208
#3/#6	Water + 6 wt% KCl + KOH	1.06	9.92	7.323×10^{-1}	3.560×10^{-2}	5.830×10^{1}	2.1461×10^{4}	1.470×10^{-3}	4.049×10^{1}	8.512

2.2.3. WRI Experiments

The standard immersion method [19] was utilized for the short-term WRI experiments under 25 °C (#1–#3) and 180 °C (#4–#6) [10]. In each group, a 350 mL solution was used to interact with a rock cube. For WRI at 25 °C, the cubes were placed in glass beakers, followed by introducing the solutions into the beakers. The beakers were sealed with covers, and the residual air in the beakers was displaced with nitrogen (N_2). Then, the WRI experiments proceeded under room conditions for 16 h. For WRI at 180 °C, the cubes were placed in high-temperature and high-pressure (HTHP) bearing vessels, and the solutions were added into the vessels. The residual air in the vessels was also displaced with N_2, after which the vessels were put into a heating oven. Subsequently, the vessels were steadily and quickly heated to 180 °C, and maintained at 180 °C for 16 h. The WRI experimental duration is referred to the test duration for recovery rate in the Chinese standard Q/SY 02408-2021 "Evaluation procedure for the inhibition and sodium/calcium tolerance of water-based drilling fluids", as the control of WRI essentially belongs to inhibition capacity of drilling fluids. After interactions, the cubes were cleaned and dried with the same method.

2.2.4. Morphological Identification

Morphological identification of the rock surfaces before and after WRI was performed to determine the induced morphological alterations. Initially, rock-surface topography of the observed surfaces was characterized using laser scanning with the VK-X1000 laser microscope from Keyence Co., Ltd., Osaka, Japan, with a resolution ratio of 0.1 nm, which is represented by the heights of all points on the scanning surfaces relative to the datum plane. The scanned region covers the entire polished surface of each rock sample, with an area of 10 mm × 10 mm. To reveal the topography alteration mechanisms, microscopic observation and mineralogical identification on the observed surfaces were carried out through scanning electron microscope and energy dispersive spectrum (SEM-EDS) using the SUPRA 55 field emission scanning electron microscope (FESEM) from Carl Zeiss AG Co., Ltd., Oberkochen, Germany, with a resolution ratio of 0.8 nm. The regions observed via FESEM before and after WRI are identical, and the alignment of these replicated regions is achieved through the positioning of characterized areas.

2.3. Hydrogeochemical Simulation of WRI

Simulations of mineral reactions between the solutions and rocks were carried out, aiming at supporting the mineralogical alterations that cause morphological alterations. The hydrogeochemical simulation was conducted using PHREEQC Interactive 3.6.2-15100, which is widely applied for calculating hydrogeochemical reactions in saline waters under various temperatures and pressures [32,33]. The solutions were defined in the Solution module, and the solution reactants were defined in the Reaction module. The temperatures were defined in the Reaction_Temperature module, and the minerals were defined in the Equilibrium_Phases module. For reaction kinetic calculations, the Phases, Rates, and Kinetics modules were used. A mineral reaction kinetic model was defined in the Rates module, in which the dissolution rate of mineral i can be expressed as follows (Equation (1)) [12]:

$$\begin{aligned} r_i &= k_i \frac{a_{0,i}}{V_{\mathrm{sol}}} \left(\frac{m_i}{m_{0,i}} \right)^{0.67} (1 - \Theta) \\ &= k_i \frac{a_0}{V_{\mathrm{sol}}} \left(\frac{n_i M_i}{n_{0,i} M_i} \right)^{0.67} (1 - 10^{\mathrm{SI}}) \\ &= k_i \frac{a_0}{V_{\mathrm{sol}}} \left(\frac{n_i}{n_{0,i}} \right)^{0.67} (1 - 10^{\mathrm{SI}}) \end{aligned} \quad (1)$$

where r is the reaction rate, k is the reaction rate constant, a_0 is the initial surface area of reactant, V_{sol} is the solution volume, m is the remaining mass of reactant, m_0 is the initial

mass of reactant, Θ is the activity quotient, n is the remaining mineral moles, n_0 is the initial mineral moles, M is the molar mass, SI is the saturation index, subscript i denotes mineral i, and subscript 0 denotes initial. k is determined by Arrhenius equation (Equation (2)) [15]:

$$k_i = k_{0,i} \exp\left(-\frac{Ea}{RT}\right) \quad (2)$$

where k_0 is the pre-exponential factor, Ea is the activation energy, T is the reaction temperature, and R is the universal gas constant, which is 8.314×10^{-3} kJ/mol·K. Additionally, a_0 is given as (Equation (3)):

$$a_0 = m_0 \mathrm{SSA} = n_0 M \mathrm{SSA} \quad (3)$$

where SSA is the specific surface area of reactant.

2.4. Roughness–Permeability Model

Surface topography alteration of the rock surfaces is quantified by rock-surface roughness, which is represented by arithmetic mean height Sa (Equation (4)) [34]:

$$Sa = \frac{1}{A} \iint_A |Z(x,y)| dxdy \quad (4)$$

where A is the projected surface area of a scanning surface, and $Z(x,y)$ is the absolute coordinate of a height within the projected surface area. The change rate of Sa is defined as η, which is given as (Equation (5)):

$$\eta = \frac{Sa' - Sa_0}{Sa_0} \cdot 100\% = \frac{\Delta Sa}{Sa_0} \cdot 100\% \quad (5)$$

where Sa' is the altered arithmetic mean height after WRI. A variation in surface roughness leads to a change in fracture permeability [35–38]. For laminar flow of incompressible fluids within single parallel fracture, assuming that the fracture surface exhibits homogeneous roughness, the roughness–permeability model can be described as (Equation (6)) [37]:

$$K = \frac{b^3 l}{12S} \cdot \frac{1}{1 + 2.792\xi^{-0.027}} \quad (6)$$

where K is the fracture permeability, b is the effective fracture aperture, l is the fracture length, S is the seepage sectional area, and ξ is the relative roughness of the fracture surface. ξ is given as (Equation (7)) [37]:

$$\xi = \frac{e}{b} = \frac{Sa}{b} \quad (7)$$

where e is the mean height of asperities on one fracture surface, which is represented by Sa, and b is the fracture aperture. S is given as (Equation (8)) [37]:

$$S = Bh \quad (8)$$

where B is the fracture width, and h is the height of seepage sectional area. A schematic diagram of the rough parallel fracture model is illustrated in Figure 1.

Combining Equations (6) and (7) gives:

$$K = \frac{b^3 l}{12S} \cdot \frac{1}{1 + 2.792(Sa/b)^{-0.027}} \quad (9)$$

Further, combining Equations (5) and (9) gives Equation (10):

$$\frac{K'}{K_0} = \frac{1+2.792(Sa_0/b)^{-0.027}}{1+2.792(Sa/b)^{-0.027}} = \frac{1+2.792(Sa_0/b)^{-0.027}}{1+2.792(Sa_0/b)^{-0.027}(1+\eta)^{-0.027}} \quad (10)$$

where the K' is the changed permeability due to surface roughness alterations. The overall research process is illustrated in Figure 2.

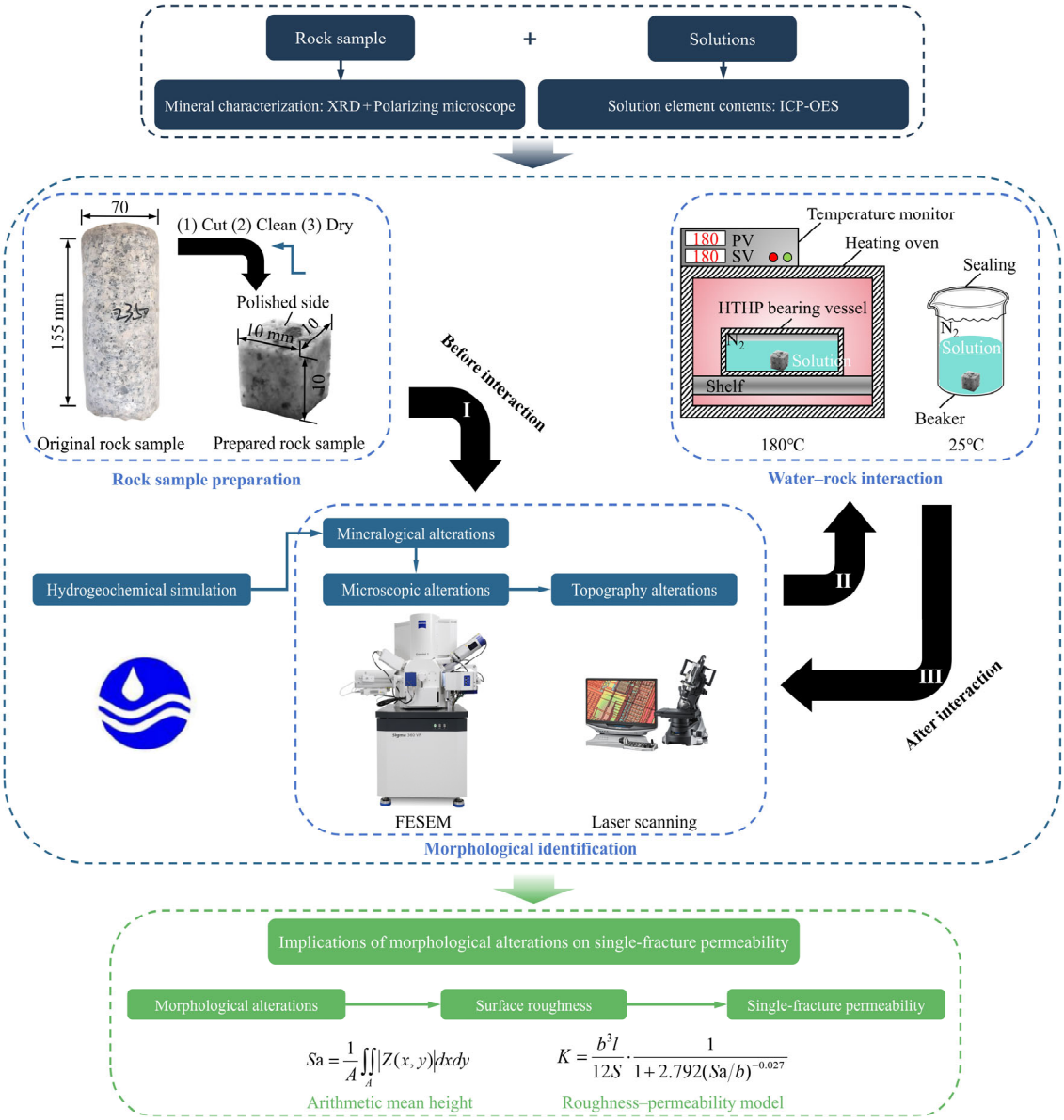


Figure 2. Schematic diagram of the overall research process.

3. Results and Discussions

3.1. Characteristics of the HDR

The prepared rock sample weighs 2.606 g on average using an electronic balance. The XRD results show that the HDR primarily contains 20 wt% quartz (Qtz), 49 wt% albite (Ab), 29 wt% microcline (Mic), and 2 wt% biotite (Bt). Based on the mineral contents, the HDR is classified as biotite monzonitic granite [39,40]. As shown in Figure 3, feldspar (Fsp), which includes Ab and Mic, Qtz and Bt were observed. The mineral grains are in close contact

with each other, indicating a tight rock matrix of the HDR. Statistical analysis of mineral grain dimension shows that the average grain dimensions of Fsp, Qtz and Bt are 446.8 μm, 235.6 μm and 292.3 μm, respectively, meanwhile the d50 of Fsp, Qtz and Bt are 349.3 μm, 137.4 μm and 277.8 μm. The mineral grain dimensions, in descending order, are Fsp, Bt and Qtz.

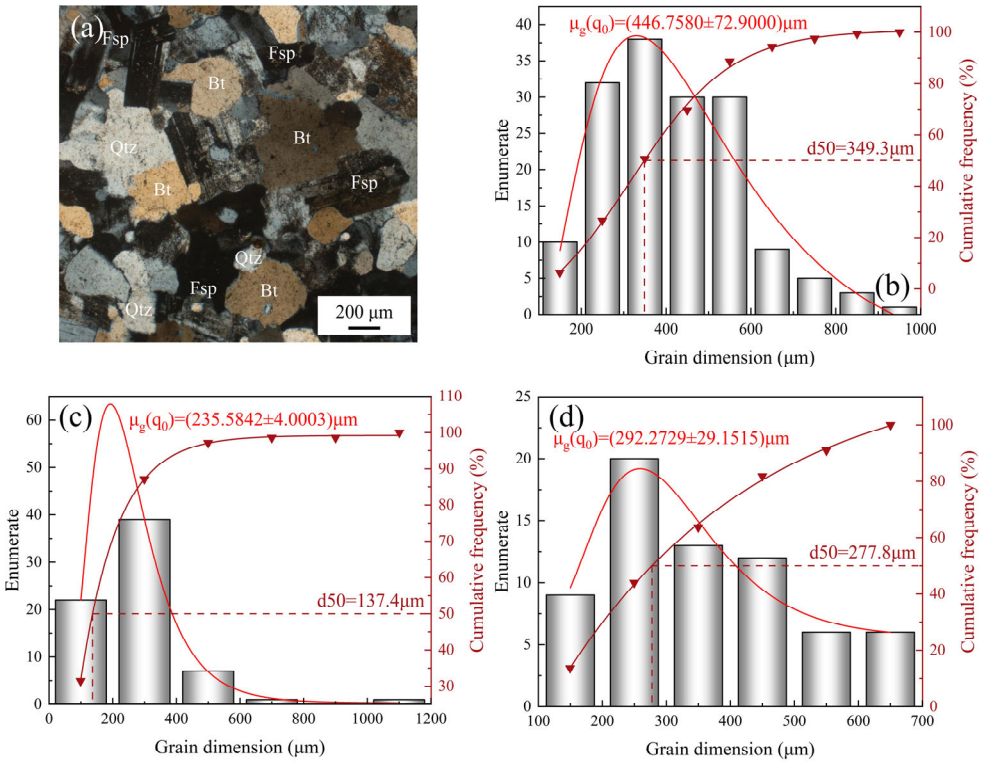


Figure 3. Mineralogical characteristics of the HDR: (**a**) picture of the HDR thin section; (**b**) grain dimension of feldspar; (**c**) grain dimension of quartz; (**d**) grain dimension of biotite.

3.2. Rock-Surface Topography Alterations and Their Mechanisms

3.2.1. Results of Rock-Surface Topography Alterations

Figure 4 qualitatively shows the topography alterations on the rock surfaces. The height values of the surface topography are influenced by the selected datum plane. This has no influence on a qualitative description of the topography across the rock surfaces and the quantitative determination of *S*a. Generally, WRI leads to obvious topography alterations on the rock surfaces, and a higher temperature significantly promotes these alterations. After WRI, the topography of rock surfaces in #1 and #3 exhibits a slight differentiation, while that in #4 and #6 shows intensified differentiation. Both phenomena suggest an increase in rock-surface roughness. In contrast, in #2 and #5, compared to the original rock surfaces, the rock surfaces become more uniform after WRI, as evidenced by the presence of similar and repeatedly occurring topography units. This indicates the homogenization of the rock-surface topography and, consequently, a reduction in rock-surface roughness. Figure 5 demonstrates a quantitative description of the topography alterations. After interaction with the water (#1 and #4) and alkaline KCl solution (#3 and #6), the *S*a of the rock surfaces increases. By contrast, a decrease in *S*a is determined after interaction with the alkaline NaCl solution (#2 and #5). The qualitative and quantitative results of the rock-surface topography alterations keep consistent.

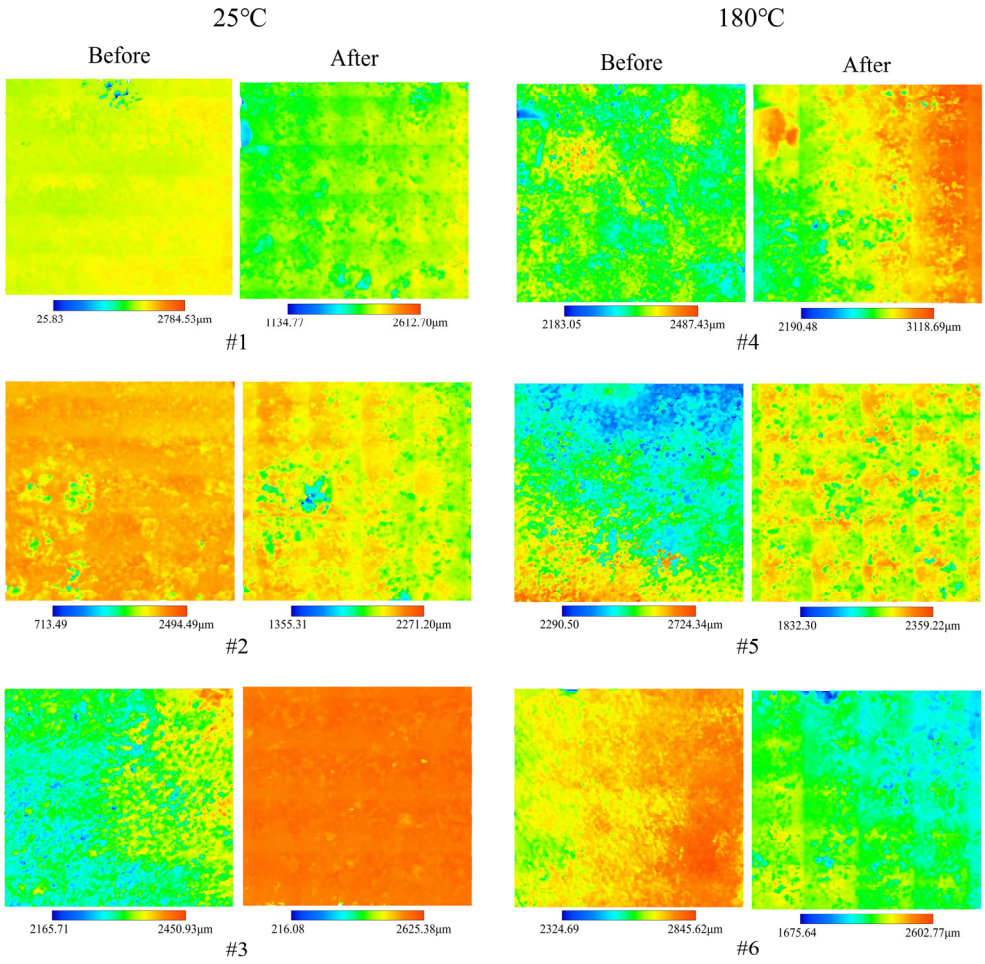


Figure 4. Topography maps on the rock surfaces in each group before and after WRI. #1 to #6 corresponds to the rock samples from WRI experiments #1 to #6 respectively.

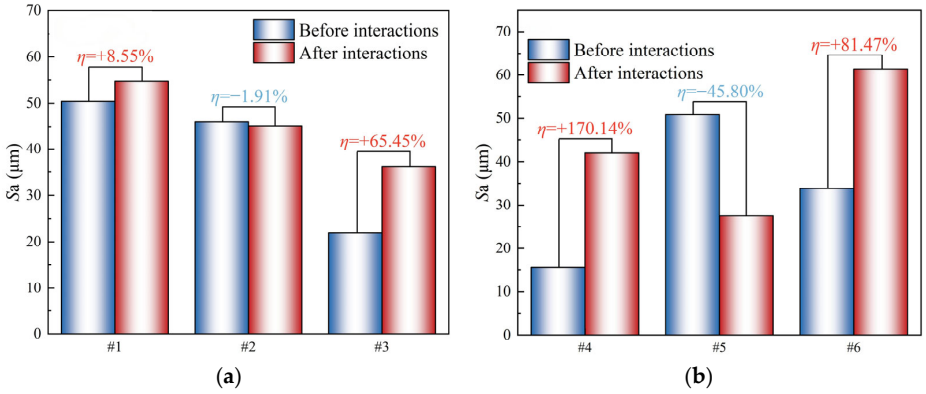


Figure 5. Changes in *Sa* on the rock surfaces in each group before and after WRI: (**a**) 25 °C; (**b**) 180 °C.

3.2.2. Morphological Alteration Mechanisms

Microscopic and mineralogical alterations on the rock surfaces are illustrated in Figure 6. Generally, the magnitude of microscopic morphological alterations on the surfaces of Bt and Fsp is more significant than that observed on Qtz. Furthermore, the roughened surface area of feldspar is larger and commonly observed. The alterations mainly contain the enlargement and generation of micro-pores and cracks on the surfaces of Bt and Fsp, as well as the precipitation of silicates. In #1, the morphological alterations are nearly negligible. In #4, generated micro-pores are observed on the Bt surfaces. In #5, similar alterations are identified, which are characterized by a large number of generated parallel

cracks on the Bt surfaces. These pores and cracks can be attributed to the opening of Bt cleavage fissures, which result from the hydrolysis dispersion of Bt induced by a low K+ concentration in the solution [41]. Additionally, the precipitation of secondary minerals is observed on the rock surfaces in #2 and #5, which belong to silicate, as evidenced by the EDS results in Figure 6b. The precipitations either grow along the pores and cracks or cover them. The precipitation of silicates is given as follows (Equation (11)):

$$\left(Na^{+} + K^{+} + Mg^{2+} + Ca^{2+} + Fe^{2+}\right) + Al(OH)_4^{-} + SiO_{2(aq)} + H_2O \rightarrow \text{silicates} \quad (11)$$

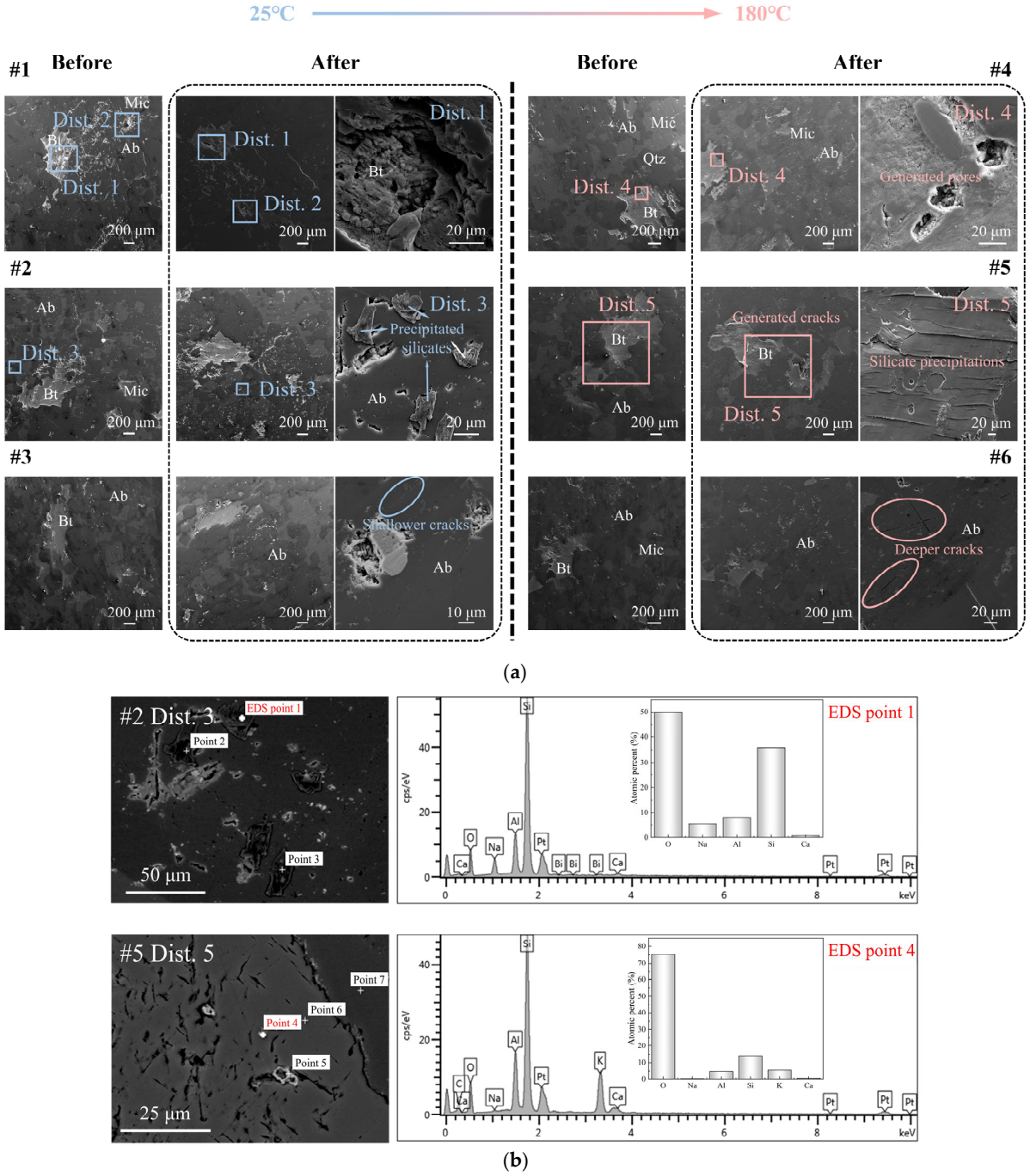


Figure 6. Microscopic and mineralogical alterations on the rock surfaces in each group: (**a**) SEM images of each group before and after WRI; (**b**) EDS results of secondary precipitations on rock surfaces.

In samples #3 and #6, no obvious pores or cracks are observed on the surfaces of Bt, indicating that a high K^+ concentration inhibits the hydrolysis dispersion of Bt. It can also be seen that the enhanced mineral dissolution at a higher temperature enlarges the cracks on the Fsp surfaces.

Figure 7 shows the smoothening and roughening mechanisms of rock surfaces. The smoothening of rock surfaces due to secondary mineral precipitations is defined as a coating effect [10,42,43]. At the initial stage of WRI, driven by chemical disequilibrium [44], the leaching of K, Na, Al, and Si from minerals into the solutions happens. The leached element contents, along with the original solution element contents, lead to increases in solution content concentrations of K, Na, Al, and Si. This promotes secondary mineral precipitate on the rock surfaces [5,45,46], which are silicates herein. These precipitations either cover or fill the pores and cracks on the rock surfaces, thereby smoothening the rock surfaces and reducing the Sa of #2 and #5. Therefore, although the generated cracks may increase the rock-surface roughness, the Sa of #5 decreases.

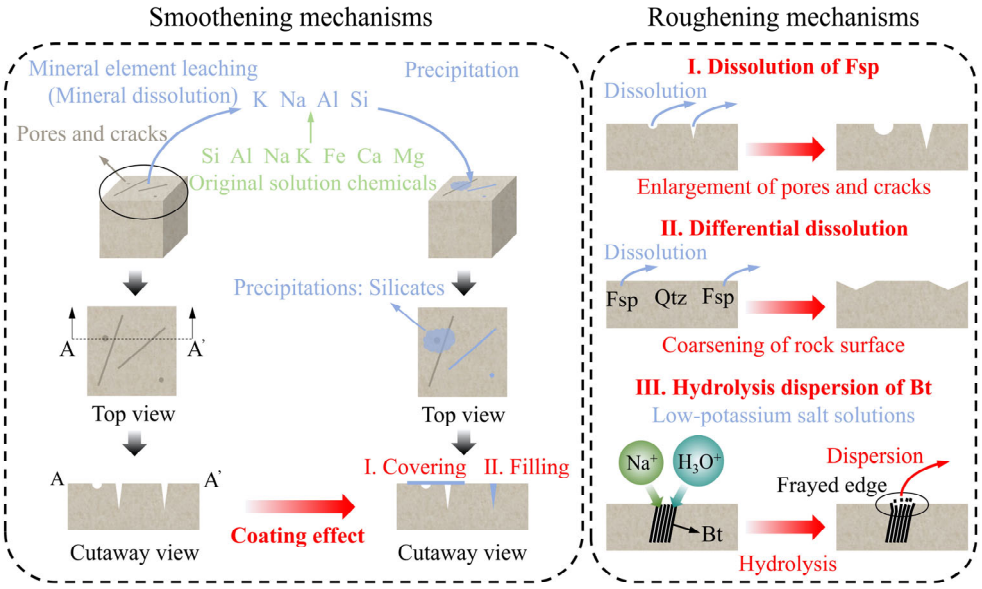


Figure 7. Schematic diagram of the morphological alteration mechanisms of the rock surfaces, including smoothening mechanisms and roughening mechanisms.

The roughening mechanisms of rock surfaces contain the dissolution of Fsp, the differential dissolution of minerals, and the hydrolysis dispersion of Bt. The dissolution of Fsp can enlarge pores and cracks on mineral surfaces, thus increasing rock-surface roughness. Due to differences in mineral reactivity, varying degrees of mineral dissolution cause differential dissolution across rock surfaces [47]. Under the reaction conditions herein, the reactivity of Fsp is significantly higher than Qtz, leading to a greater amount of dissolved Fsp and a smaller amount of dissolved Qtz. This coarsens rock surfaces and further increases the rock-surface roughness. In #1, #2, #4, and #5, a low potassium content in the solutions results in the hydrolysis dispersion of Bt on the rock surfaces. The hydrated cations in the solutions, including Na^+ and H_3O^+, exchange with the K^+ in Bt. As hydrated Na^+ and H_2O are larger than K^+, the entering of hydrated cations from the edges of Bt into the interlayers of Bt crystals causes an increase in the interlayer spacing of the Bt crystal [48]. This results in the opening of Bt cleavage fissures, which is represented by the frayed edges of Bt. Subsequently, fines will detach from the frayed edges, enlarging or generating pores and cracks on the surfaces of Bt [49]. The radius of hydrated Na^+ is larger than that of H_2O, and hence the hydrolysis dispersion of Bt in #5 is significantly more intensified compared with that in #4. Notwithstanding this typical morphological alteration on the Bt surface, the

Fsp dissolution and differential dissolution among minerals contribute more substantially to the roughening of rock surfaces. This is because morphological alterations are pervasive and cover a larger proportion of the total rock surface area. Accordingly, the rock surfaces in #3 and #6 still exhibited significant roughening, even when the hydrolysis dispersion of Bt was inhibited.

3.3. Hydrogeochemical Simulation Results

During simulations, Mic is represented by K-feldspar (Kfs), and Bt is represented by K-mica in the database of PHREEQC. Given the low biotite content in the rock sample and its non-reactivity within the experimental conditions adopted in this study [50], the representing of K-mica by biotite has a negligible influence on the simulation results. The simulation parameters of WRI are listed in Table 3.

Table 3. Simulation parameters of WRI.

Parameters	Units	Minerals			
		Ab	Kfs	Qtz	K-mica
Chemical formulas		$NaAlSi_3O_8$	$KAlSi_3O_8$	SiO_2	$KAl_3Si_3O_{10}(OH)_2$
Molar mass	g/mol	262	278	60	398
Initial moles, m_0	mol	4.874×10^{-3}	2.718×10^{-3}	8.687×10^{-3}	1.310×10^{-4}
Specific surface area, SSA [1,2]	m^2/g	0.056	0.254	0.633	0.510
Pre-exponential factor, k_0 [2]	$mol/m^2 \cdot s$	3.91×10^{-4}	1.28×10^{-5}	276	1.01×10^{-7}
Activation energy, Ea [2]	kJ/mol	50.7	38	90.1	22

[1] The specific surface area of Ab and Kfs is referred to [12]. [2] The specific surface area of K-mica, and the pre-exponential factor and activation energy of the minerals are referred to [15]. The specific surface area of Qtz is inferred from those of other minerals based on grain dimensions.

Figure 8 shows the simulation results of the kinetics of mineral reactions within elapsed experimental time. Generally, a higher temperature significantly accelerates the mineral dissolution. Kfs is the most reactive mineral. The amount of dissolved minerals, in descending order, is Kfs, K-mica, Ab and Qtz at 25 °C, and is Kfs, Ab, K-mica and Qtz at 180 °C. This is because the dissolution of Fsp increases significantly more than that of K-mica with rising temperatures. The dissolution of Ab, Kfs, K-mica and Qtz is given as follows (Equations (12)–(15)) [50–52]:

$$NaAlSi_3O_8(Ab) + 2H_2O \rightarrow Na^+ + Al^{3+} + 4OH^- + 3SiO_{2(aq)} \quad (12)$$

$$KAlSi_3O_8(Kfs) + 2H_2O \rightarrow K^+ + Al^{3+} + 4OH^- + 3SiO_{2(aq)} \quad (13)$$

$$KAl_3Si_3O_{10}(OH)_2(K\text{-mica}) + 4H_2O \rightarrow K^+ + 3Al^{3+} + 3SiO_{2(aq)} + 10OH^- \quad (14)$$

$$SiO_2(Qtz) \rightarrow SiO_{2(aq)} \quad (15)$$

The simulations of mineral reaction kinetics reveal that the differences in mineral reactivity result in a different reacted amount of minerals, thereby leading to differential mineral dissolution on rock surfaces and an increase in rock-surface roughness (e.g., [16]). To further elucidate the reaction mechanisms, simulations of reaction equilibrium between the HDR minerals and solutions were conducted, and the results are given in Figure 9. When reaction equilibrium is reached, the content of Fsp decreases, while the contents of Bt and Qtz increase. This indicates that under the experimental conditions in this study,

Fsp tends to dissolve compared to Qtz and Bt from the perspective of thermodynamics. Since the dissolved amount of Bt is substantially lower than that of feldspar and Bt tends to precipitate, the morphological alteration induced by Bt is dominated by hydrolysis dispersion. The inhibition of Kfs dissolution reduces the precipitation of K-mica and Qtz, which implies that the dissolution of Fsp provides Al and Si for the precipitation of K-mica and Qtz [10,39]. The dissolution and precipitation of minerals are a dynamic equilibrium process. Although Bt has an overall tendency to precipitate, short-term dissolution of Fsp cannot provide sufficient solutes for Bt precipitation, and hence Bt experiences slight dissolution in the early stage.

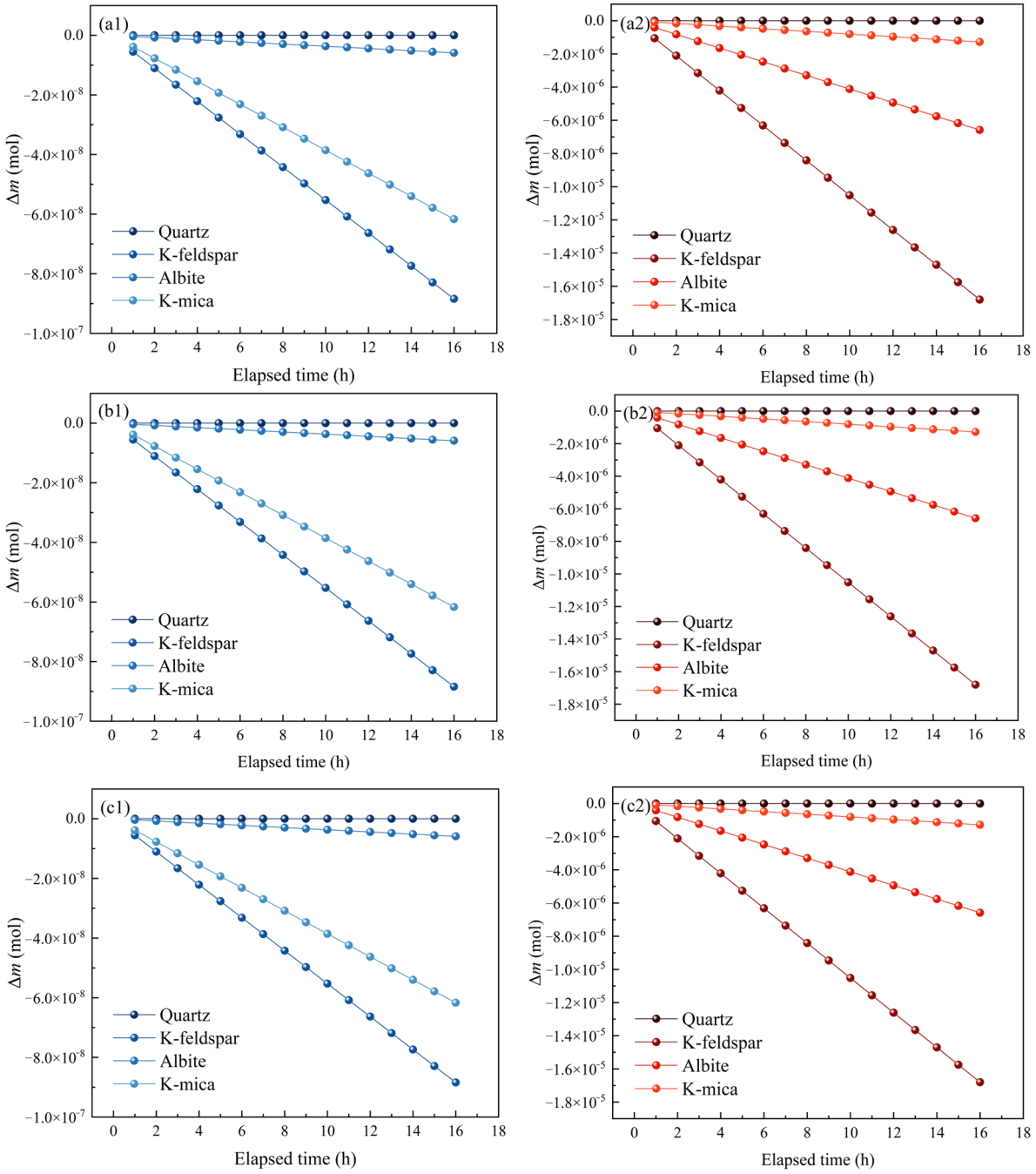


Figure 8. Simulation results of kinetics of mineral reaction within elapsed experiment time: (**a1**,**a2**) pure water; (**b1**,**b2**) NaCl + NaOH (pH = 10); (**c1**,**c2**) KCl + KOH (pH = 10). Number 1 denotes temperature of 25 °C, and number 2 denotes temperature of 180 °C.

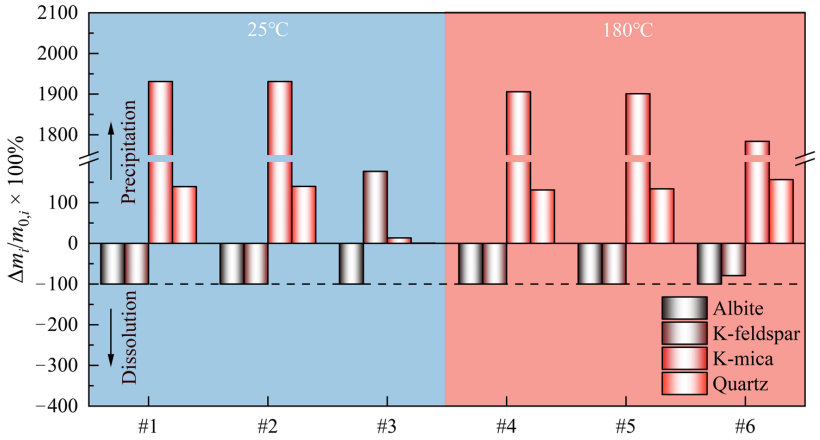


Figure 9. Simulation results of reaction equilibrium between the HDR minerals and solutions. Δm_i is the changed mass of mineral i, and $m_{0,i}$ is the initial mass of mineral i. The blue background color corresponds to simulations performed at 25 °C, and the red background color corresponds to simulation performed at 180 °C.

3.4. Implications of Morphological Alterations on Single-Fracture Permeability

3.4.1. Validation of Numerical Calculation Model

The numerical calculation model, namely, the roughness–permeability model, is shown in Equation (9). To verify the rationality and applicability of the model, parallel rough-fracture seepage experiment data collected from Ref. [37] was adopted to compare with the permeability values through theoretical calculations based on the model. The relative errors (δ) between theoretical values and experimentally determined values are calculated by Equation (16):

$$\delta = \frac{|K_e - K|}{K} \times 100\% \quad (16)$$

where K_e is the experimentally determined permeability. Table 4 gives the specific parallel rough-fracture seepage experiment data, and Figure 10 shows the comparison between the theoretically calculated permeability and experimentally determined permeability.

Table 4. Parallel rough-fracture seepage experiment data.

No.	S (m^2)	l (m)	ξ	b (μm)	K_e (μm^2)	Reference
1	0.04	0.2	0.800	50	0.015	[37]
2			0.400	100	0.120	
3			0.267	150	0.989	
4			0.200	200	2.588	
5			0.133	300	8.398	

Figure 10 indicates that when the fracture aperture is less than 100 μm, the model can effectively predict permeability, with the relative error around 10 %. Nevertheless, with the fracture aperture increase from 100 μm to 150 μm, the relative error increases sharply, and continues to rise with further increases in the fracture aperture. This could be attributed to the transition of the flow regime from laminar to turbulent flow. The opening of the fracture aperture weakens the restrictive effect of the flow boundaries, namely, the rough rock surfaces, on fluid flow within fractures, which enhances the inertial effect. The enhanced inertial effect promotes the flow regime transition from laminar flow to turbulent flow [53]. Given that the roughness–permeability model is merely valid under laminar flow conditions, this transition renders the model inapplicable. Therefore, the roughness–permeability model can only be applied to predict the permeability of fractures with a (mechanical) aperture of less than 100 μm.

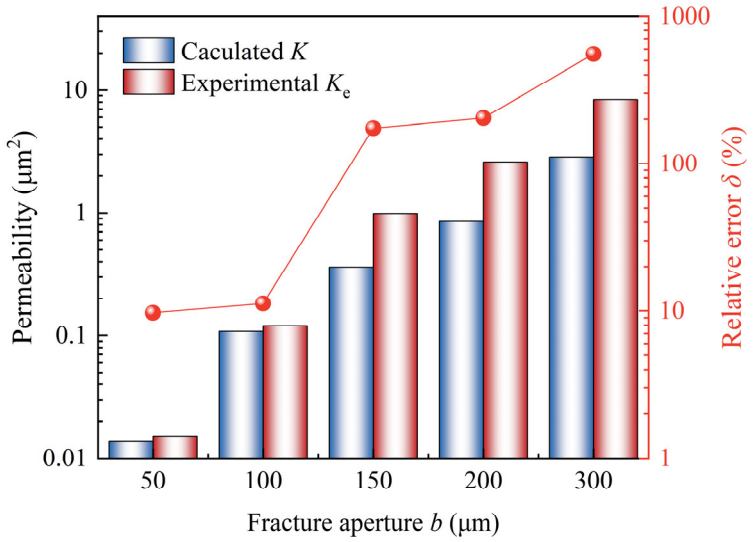


Figure 10. Comparison between the theoretically calculated permeability and experimentally determined permeability.

3.4.2. Predictions of Permeability Changes Due to Morphological Alteration

Fracture permeability plays a crucial role in the productivity of HDR geothermal reservoirs [9]. The roughness of rock-fracture surfaces has an important influence on fracture seepage characteristics, especially fracture permeability [35]. Based on Equation (10), the permeability alterations due to WRI between the HDR and different alkaline salt solutions under 25 °C and 180 °C are presented in Figure 11. A single fracture with a aperture of 100 μm is considered. During calculation, the fracture aperture is assumed to be constant. The results show that fracture permeability increases as *S*a increases and decreases as *S*a decreases. This is because, when the fracture aperture is fixed, an increase in *S*a enlarges the seepage channel space, thereby increasing fracture permeability. On the contrary, a decrease in *S*a narrows the seepage channel space, leading to a fracture permeability reduction [13,38]. The mechanisms are demonstrated in Figure 12. Additionally, the enhanced alterations in *S*a promote the fracture permeability alterations.

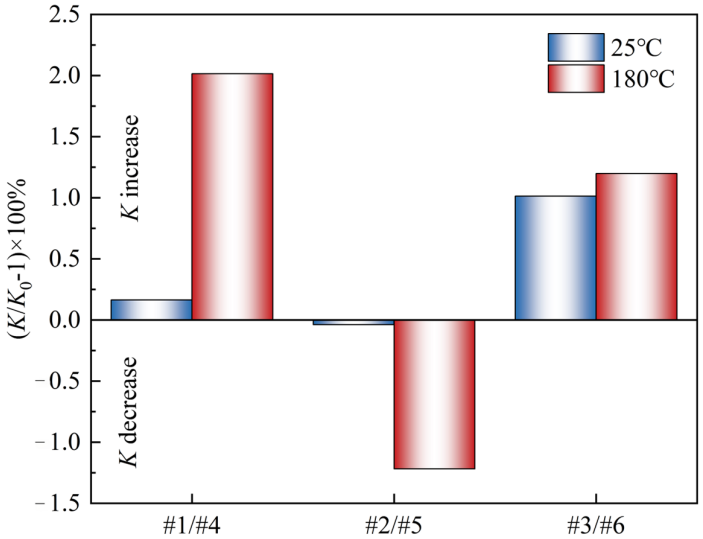


Figure 11. Predicted single-fracture permeability changes due to morphological alterations induced by WRI.

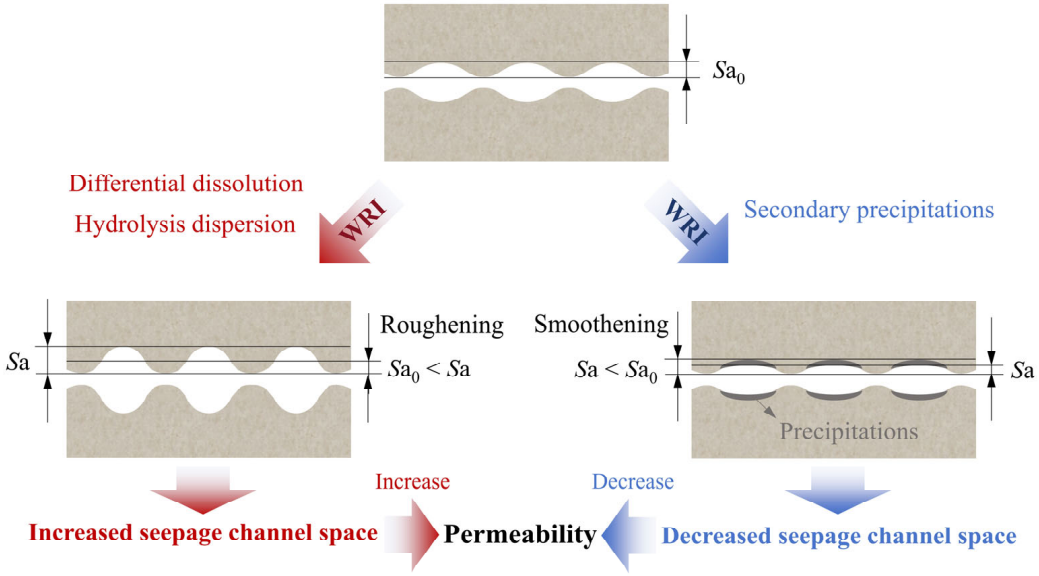


Figure 12. Schematic diagram of single-fracture permeability change mechanisms due to morphological alterations induced by WRI.

3.4.3. Permeability Changes Due to Various Fracture Parameters

Based on the roughness–permeability model (Equation (9)), the changes in permeability caused by various fracture parameters before and after WRI in the alkaline KCl solution under 180 °C (#6) are taken as the numerical calculation example (Sa_0 = 33.84 μm, Sa = 61.41 μm). The numerical calculation results are shown in Figure 13. Model parameters of the fractures along with their values are presented in Table 5.

Table 5. Model parameters of the fractures and their values.

Items	Units	Values
Arithmetic mean height, Sa	μm	33.84 μm (Sa_0), 61.41 μm (Sa)
Fracture aperture, b	μm	61.41–100
Fracture width, B	m	0.01–0.1
Fracture section area height, h	m	0.02
Fracture length, l	m	0.01–0.1

The results elucidate that fracture permeability is positively correlated with the fracture aperture b and fracture length l, while it is negatively correlated with fracture width B. The differences between fracture permeability before and after WRI are intensified by an increase in the values of b and l. Fracture width B has a negligible influence on fracture permeability before and after WRI. The influence of fracture parameter changes on fracture permeability alterations induced by surface roughness variations is essentially attributed to changes in the effective fracture aperture resulting from the surface roughness variations. The decrease in B and the increase in l directly change the fracture surface area. The fracture permeability within the increased fracture surface area is influenced by the effective aperture alterations induced by rock-surface roughness alterations, and hence the alterations in fracture permeability are enhanced.

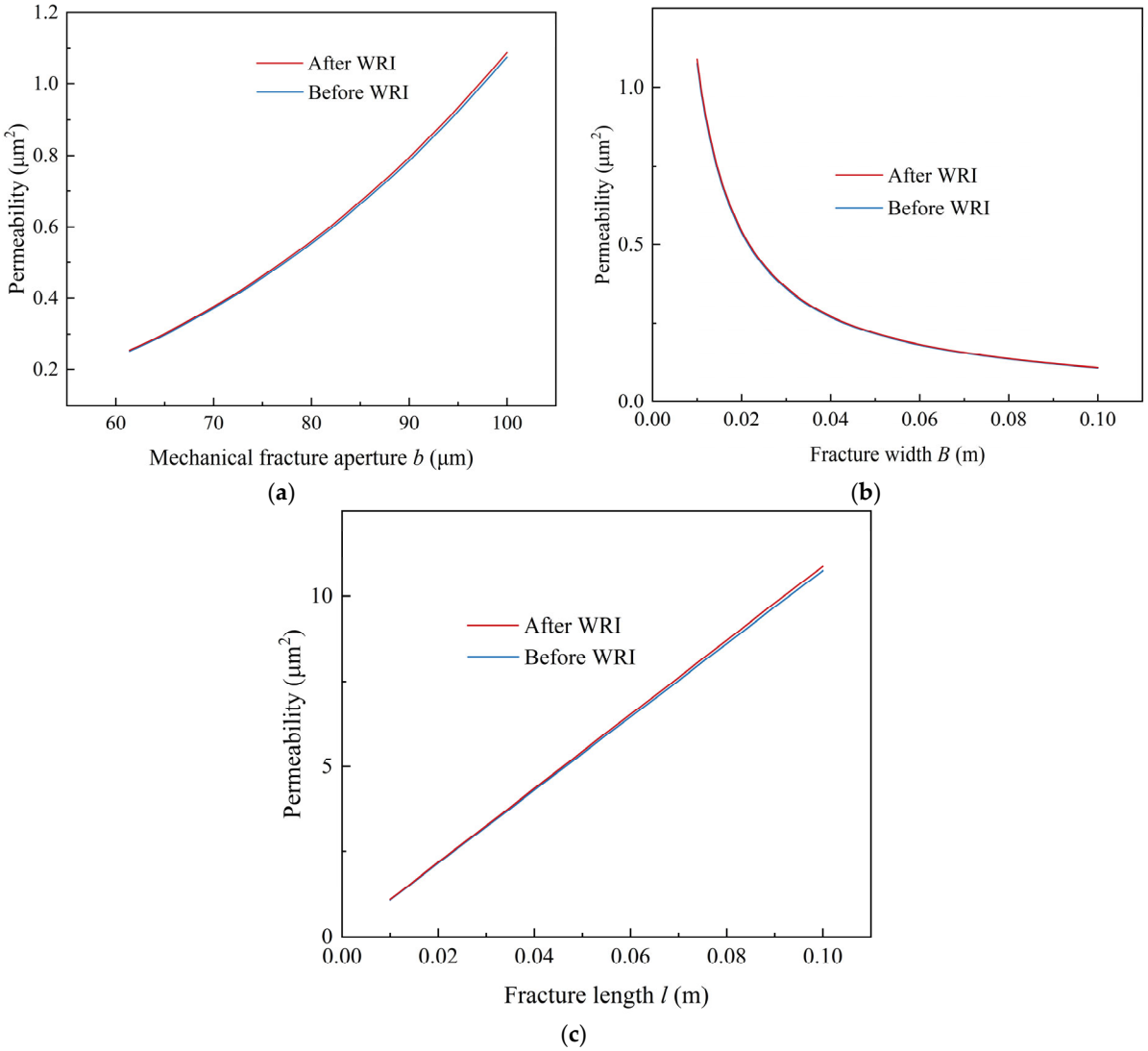


Figure 13. Permeability alterations due to various fracture parameters before and after WRI in alkaline KCl solution under 180 °C: (**a**) fracture aperture *b*; (**b**) fracture width *B*; (**c**) fracture length *l*.

4. Conclusions

In this study, short-term (16 h) WRI experiments between the HDR and three reactive solutions, pure water, the alkaline 6 wt% NaCl solution (pH = 10) and the alkaline 6 wt% KCl solution (pH = 10), were carried out. The morphological alterations on the rock surfaces and their mechanisms were investigated. Based on the roughness–permeability model, the implication of morphological alterations on fracture permeability was revealed. The main findings are drawn as follows:

1. Short-term WRI between the granitic HDR and the reactive solutions can lead to morphological alterations on the rock surfaces. The alkaline 6 wt% NaCl solution leads to smoothening of the rock surfaces, while pure water and the alkaline 6 wt% KCl solution cause roughening. A higher temperature promotes these morphological alterations. The smoothening of the HDR surfaces results from a coating effect due to secondary silicate precipitations. Initially, K, Na, Al, and Si leach out from the minerals into solutions, which induces silicate precipitations. These precipitations either cover or fill the pores and cracks on the rock surfaces. The roughening mechanisms of the rock surfaces contain the dissolution of Fsp, the differential dissolution between minerals, and the hydrolysis dispersion of Bt. Fsp dissolution causes the enlargement

of pores and cracks, and the differential dissolution of minerals causes the coarsening of rock surfaces. The hydrolysis dispersion of Bt, which is attributed to a low K^+ concentration in solutions, enlarges and generates pores and cracks on the Bt surfaces.

2. With a fracture aperture less than 100 μm, the smoothening and roughening of rock surfaces led to a decrease and an increase in fracture permeability, respectively. Considering a fixed fracture aperture, the precipitations that cause the smoothening narrow the seepage channel space, leading to a permeability reduction. The dissolution and hydrolysis dispersion of minerals enlarge the seepage channel space, and hence increase fracture permeability. For the millimetric to centimetric scale range of the rock sample size in this study, these morphological alterations enhance the influence of fracture parameters, including fracture length (l) and fracture aperture (b), on fracture permeability. This study mainly focuses on the influences of seepage channel space changes due to WRI on a single rough parallel fracture with homogeneous fracture surface roughness. Nevertheless, factors including the contact area, aperture distribution, fracture tortuosity, mechanical closure, mineral infilling, and stress conditions also exert notable influences on fracture permeability, necessitating further investigations.
3. This study demonstrates that short-term WRI between the HDR and the alkaline salt solution can influence fracture permeability by altering the rock-surface roughness. The alkaline 6 wt% NaCl solution reduces the fracture permeability by smoothening the rock surfaces. By contrast, the alkaline 6 wt% KCl solution increases the fracture permeability by roughening the rock surfaces, and can inhibit Bt hydrolysis dispersion, which might lead to fines migration. From the perspective of WRI inhibition, the alkaline 6 wt% KCl solution has a better reservoir protection capacity. It should be noted that the salts and pH regulators jointly influence WRI in this study. In future works, the salinity effect and pH effect can be separately investigated to better understand the WRI regulating mechanisms. Furthermore, the D&C fluids have much more complex compositions, which could also participate in WRI through distinct mechanisms.
4. Owing to the limitations of the equipment, only small-scale morphological alterations on the rock surfaces were identified. Nevertheless, the relationships among mineral alterations, morphological alterations, and permeability changes provide insights into the elimination of HDR reservoir damage from the perspective of optimizing fluid contents. Given that fluid transport in geothermal reservoirs is governed by complex fracture networks, extrapolating the results from a single fracture to reservoir-scale permeability requires additional justification or numerical validation.

Supplementary Materials: The following supporting information can be downloaded at: https://www.mdpi.com/article/10.3390/app16178622/s1, S1: Simulation program for mineral reaction kinetics; S2: Simulation program for mineral reaction equilibrium.

Author Contributions: Conceptualization, O.J. and X.Z.; methodology, O.J.; software, O.J.; validation, O.J. and X.Z.; formal analysis, O.J. and R.Z.; investigation, O.J. and P.Z.; resources, D.H., X.Z. and Y.F.; data curation, P.Z. and R.Z.; writing—original draft preparation, O.J. and R.Z.; writing—review and editing, X.Z. and R.Z.; visualization, O.J.; supervision, X.Z. and Y.F.; project administration, X.Z., D.H. and Y.F.; funding acquisition, D.H., X.Z. and Y.F. All authors have read and agreed to the published version of the manuscript.

Funding: This research was funded by the Deep Earth Probe and Mineral Resources Exploration–National Science and Technology Major Project, grant number 2024ZD1003506, the National Natural Science Foundation of China, grant number 42172342, the Science and Technology Innovation Special Project of Xiong'an New Area, grant number 2022XAGG0500, and the Science and Technology (S&T)

Program of Hebei Province, grant number 235A4601D. The APC was funded by the National Natural Science Foundation of China, grant number 42172342.

Institutional Review Board Statement: Not applicable.

Informed Consent Statement: Not applicable.

Data Availability Statement: The original contributions presented in the study are included in the article/Supplementary Materials, further inquiries can be directed to the corresponding author.

Acknowledgments: We thank Yongming Yang from Hebei Weiye Geothermal New Energy Technology Co., Ltd. for his support to this work.

Conflicts of Interest: The author Mr. Yousheng Feng was employed by the company Hebei Weiye Geothermal New Energy Technology Co., Ltd. Author Dehua Hu was employed by the company China National Nuclear Corporation. Author Renjie Zhang was employed by the company PetroChina Dagang Oilfield Company. The remaining authors declare that the research was conducted in the absence of any commercial or financial relationships that could be construed as a potential conflict of interest.

Abbreviations

The following abbreviations are used in this manuscript:

Albite	Ab
Biotite	Bt
EGS	Enhanced Geothermal System
Feldspar	Fsp
HDR	Hot Dry Rock
HTHP	High-Temperature and High-Pressure
Kfs	K-feldspar
Microcline	Mic
Quartz	Qtz
SI	Saturation Index
WRI	Water–Rock Interaction

References

1. Wang, G.L.; Zhang, W.; Ma, F.; Lin, W.J.; Liang, J.Y.; Zhu, X. Overview on hydrothermal and hot dry rock researches in China. *China Geol.* **2018**, *2*, 273–285. [CrossRef]
2. Wang, J.Y.; Pang, Z.H.; Cheng, Y.Z.; Huang, Y.H.; Jiang, G.Z.; Lu, Z.N.; Kong, Y.L. Current state, utilization and prospective of global geothermal energy. *Sci. Technol. Rev.* **2023**, *41*, 5–11.
3. Xu, T.F.; Hu, Z.X.; Li, S.T.; Jiang, Z.J.; Hou, Z.Y.; Li, F.Y.; Liang, X.; Feng, B. Enhanced geothermal system: International progresses and research status of China. *Acta Geol. Sin.* **2018**, *92*, 1936–1947.
4. Hou, Z.M.; Wu, X.N.; Luo, J.S.; Zhang, L.H.; Li, Z.Y.; Cao, C.; Wu, L.; Chen, Q.J. Major challenges of deep geothermal systems and an innovative development mode of REGS integrated with energy storage. *Coal Geol. Explor.* **2024**, *52*, 1–13.
5. Gao, B.B.; Li, Y.M.; Pang, Z.H.; Huang, T.M.; Kong, Y.L.; Li, B.; Zhang, F. Geochemical mechanisms of water/CO_2-rock interactions in EGS and its impacts on reservoir properties: A review. *Geothermics* **2024**, *118*, 102923. [CrossRef]
6. He, M.; Gong, W.Z.; Xu, M.B.; Song, J.J. Research status and prospect analysis of hot dry rock development technology. *Renew. Energy Resour.* **2021**, *39*, 1447–1454.
7. Li, Y.S.; Duan, C.Y.; Zheng, X.H. Best practices for high temperature geothermal drilling. *Geol. Explor.* **2016**, *52*, 173–181.
8. Nie, D.J.; Liu, G.; Du, Z.Q.; Wu, Q.H. Study on high-temperature recyclable foam drilling fluid system for HDR drilling. *Appl. Chem. Ind.* **2023**, *52*, 2542–2546.
9. Yuan, B.; Wood, D.A. A Holistic Review of geosystem damage during unconventional oil, gas and geothermal energy recovery. *Fuel* **2018**, *227*, 99–110. [CrossRef]
10. Jiang, O.; Zheng, X.H.; Gong, Q.J.; Wu, H.D.; Chu, B.Z. Research on mass transfer mechanisms due to short-term water-rock interactions between granite cuttings and alkaline NaCl solution and their patterns. *Geoenergy Sci. Eng.* **2025**, *245*, 213512. [CrossRef]

11. Jiang, O.; Zheng, X.H.; Liu, H.Y.; Zhu, W.X.; Wu, H.D. Simulation study on the influence of reactions between granitic hot dry rock minerals and water on rock non-closed crack compressive shear initiation. *Appl. Sci.* **2025**, *15*, 9695. [CrossRef]
12. Holmslykke, H.D.; Weibel, R.; Olsen, D.; Anthonsen, K.L. Geochemical reactions upon injection of heated formation water in a danish geothermal reservoir. *ACS Earth Sci. Space Chem.* **2023**, *7*, 1635–1647. [CrossRef]
13. Tan, Q.G.; You, L.J.; Kang, Y.L.; Xu, C.Y. Formation damage mechanisms in tight carbonate reservoirs: The typical illustrations in Qaidam Basin and Sichuan Basin, China. *J. Nat. Gas. Sci. Eng.* **2021**, *95*, 104193. [CrossRef]
14. Ma, K.; Jiang, H.Q.; Li, J.J.; Zhao, L. Experimental study on the micro alkali sensitivity damage mechanism in low-permeability reservoirs using QEMSCAN. *J. Nat. Gas. Sci. Eng.* **2016**, *36*, 1004–1017. [CrossRef]
15. Yasuhara, H.; Kinoshita, N.; Ohfuji, H.; Lee, D.S.; Nakashima, S.; Kishida, K. Temporal alteration of fracture permeability in granite under hydrothermal conditions and its interpretation by coupled chemo-mechanical model. *Appl. Geochem.* **2011**, *26*, 2074–2088. [CrossRef]
16. Qiao, L.P.; Huang, A.D.; Wang, Z.C.; Gao, W.Y.; Liu, J. Alteration of minerals and temporal evolution of solution in reactive flow through granitic rock fractures. *Int. J. Rock Mech. Min. Sci.* **2019**, *123*, 104105. [CrossRef]
17. Sanchez-Roa, C.; Saldi, G.D.; Mitchell, T.M.; Iacoviello, F.; Bailey, J.; Shearing, P.R.; Oelkers, E.H.; Meredith, P.G. The role of fluid chemistry on permeability evolution in granite: Applications to natural and anthropogenic systems. *Earth Planet. Sci. Lett.* **2021**, *553*, 116641. [CrossRef]
18. Chen, Y.; Cao, P.; Pu, C.Z.; Liu, Y.K.; Li, N. Experimental study of effect of water-rock interaction on micro-topography of rock surface. *Rock Soil Mech.* **2010**, *31*, 3452–3458.
19. Pang, J.; Wu, T.T.; Yu, X.N.; Zhou, C.X.; Chen, H.T.; Gao, J.A. The effect of water-rock interaction on shale reservoir damage and pore expansion. *Processes* **2025**, *13*, 1265. [CrossRef]
20. Yang, S.G.; Yu, Q.C. The role of fluid-rock interactions in permeability behavior of shale with different pore fluids. *Int. J. Rock Mech. Min. Sci.* **2022**, *150*, 105023. [CrossRef]
21. Jiang, O.; Cao, L.; Zhu, W.X.; Zheng, X.H. Review of reservoir damage mechanisms induced by working fluids and the design principles of reservoir protection fluids: From oil-gas reservoirs to geothermal reservoirs. *Energies* **2024**, *17*, 4895. [CrossRef]
22. Huang, C.; Kang, Y.L.; You, L.J.; Li, X.L.; Tan, W.X.; Bai, R.T. Research on stress sensitivity of fracture-hole carbonate reservoirs under drilling fluid immersion. *Geoenergy Sci. Eng.* **2024**, *233*, 212537. [CrossRef]
23. Wang, G.C.; Liu, W.C.; Ren, Y.; Wang, X.L.; Xiong, K.J.; Luo, H.; Wang, L.R.; Xiao, H. A highly inhibitive low activity brine-based drilling fluid. *Drill. Fluid Complet. Fluid* **2025**, *42*, 503–508.
24. Wang, Z.H.; Shen, L.; Song, Z.K. Applied research of salt brine drilling fluid in Qinghai sylvinite strata drilling. *Coal Geol. China* **2015**, *27*, 55–58.
25. Jia, W.F.; Song, J.J.; Lin, J.; Ren, R.K.; Chen, X.; Xian, C.G. Research and performance evaluation of workover fluid based on ultra-high salinity brine. *Spec. Petrochem.* **2026**, *43*, 60–63.
26. Cao, L.; Yu, P.Z. Research and application of activity regulator in low activity water-based drilling fluids system. *Appl. Chem. Ind.* **2022**, *51*, 2344–2347+2361.
27. Baumgärtner, J.; Gérard, A.; Baria, R. Soultz-Sous-Forets: Main technical aspects of deepening the Well GPK2. In Proceedings of the World Geothermal Congress, Kyushu-Tohoku, Japan, 28 May–10 June 2000.
28. Feng, Q.; Yin, X.W.; Zhu, M.; Zhang, J.T.; Liu, W.; Xi, H.Y.; Yu, T.F.; Yang, L.S.; Liu, W.; Lu, Z.X. Overall promotion of integrated management and utilization of saline-alkali land in northwest China: Conditions, challenges, and recommendations. *Bull. Chin. Acad. Sci.* **2024**, *39*, 2060–2073.
29. Zhang, L.Y.; Li, X.F.; Zhu, G.L.; Zhang, S.S.; Zhang, C.; Wang, H.; Feng, Q.D.; Xu, W.H.; Niu, Z.X.; Deng, Z.H. Geothermal geological characteristics, genetic model and resource potential of hot dry rocks in the Gonghe Basin, Qinghai. *Geol. China* **2025**, *52*, 399–415.
30. Ma, Y.H.; Tang, B.C.; Su, S.Y.; Zhang, S.S.; Li, C.Y. Geochemical characteristics of geothermal fluids and water-rock interaction in geothermal reservoirs in and around the Gonghe Basin, Qinghai Province. *Earth Sci. Front.* **2020**, *27*, 123–133.
31. Yan, J.N. *Principle of Drilling Fluid Technology*, 1st ed.; China University of Petroleum Press: Dongying, China, 2014.
32. Appelo, C.A.J. Principles, caveats and improvements in databases for calculating hydrogeochemical reactions in saline waters from 0 to 200 °C and 1 to 1000 atm. *Appl. Geochem.* **2015**, *55*, 62–71. [CrossRef]
33. Zhao, Y.H.; Feng, B.; Zhang, G.B.; Shangguan, S.T.; Qi, X.F.; Li, X.; Qiao, Y.C.; Xu, J.N. Study of the interaction between the granitic hot-dry rock (HDR) and different injection waters. *Acta Geol. Sin.* **2020**, *94*, 2115–2123.
34. Chen, Y.; Cao, P.; Mao, D.W.; Pu, C.Z.; Fan, X. Morphological analysis of sheared rock with water-rock interaction effect. *Int. J. Rock Mech. Min. Sci.* **2014**, *70*, 264–272. [CrossRef]
35. Li, Z.H.; Chen, S.J. Numerical simulation of seepage characteristics of fractures with different roughness. *Min. Saf. Environ. Prot.* **2021**, *48*, 6–11.
36. Gan, L.; Liu, Y.; Zhang, Z.L.; Shen, Z.Z.; Ma, H.Y. Roughness characterization of rock fracture and its influence on fracture seepage characteristics. *Rock Soil Mech.* **2023**, *44*, 1585–1592. [CrossRef]

37. Lu, Z.G.; Yao, J.; Wang, D.S.; Li, L.F. Correction of cubic law and calculation of critical velocity in parallel fractures. *Res. Explor. Lab.* **2010**, *29*, 14–16+165.
38. Zhao, M.K.; Kong, D.S. Study on Seepage Characteristics of rock fractures considering fracture surface roughness and opening fractal dimension. *Chin. J. Rock Mech. Eng.* **2022**, *41*, 1993–2002.
39. Jiang, O.; Ma, L.Y.; Hou, D.R.; Zhang, P.X.; Zheng, X.H. Simulation research of chemical reactions between granitic hot dry rock and mixed injection fluids. *Appl. Chem. Ind.* **2026**, *55*, 835–840+864.
40. Lei, Z.H.; Zhang, Y.J.; Yu, Z.W.; Hu, Z.J.; Li, L.Z.; Zhang, S.Q.; Fu, L.; Zhou, L.; Xie, Y.Y. Exploratory research into the enhanced geothermal system power generation project: The Qiabuqia Geothermal Field, Northwest China. *Renew. Energy* **2019**, *139*, 52–70. [CrossRef]
41. Xin, X.J.; Zhao, F. Biotite hydration mechanism and the influence on water injection production. *J. Southwest Pet. Univ. (Sci. Technol. Ed.)* **2009**, *31*, 81–84.
42. Pollet-Villard, M.; Bouissonnié, A.; Schäfer, G.; Ackerer, P.; Fritz, B.; Cabié, M.; Daval, D. Impact of secondary coatings on the dissolution rate of K-feldspar: A combined experimental and modeling study. *Geothermics* **2024**, *119*, 102952. [CrossRef]
43. Civan, F. Formation damage mechanisms and their phenomenological modeling—An overview. In Proceedings of the SPE Formation Damage Conference, Scheveningen, The Netherlands, 30 May–1 June 2007.
44. Savage, D.; Bateman, K.; Milodowski, A.E.; Hughes, C.R. An experimental evaluation of the reaction of granite with streamwater, seawater and NaCl solutions at 200 °C. *J. Volcanol. Geotherm. Res.* **1993**, *57*, 167–191. [CrossRef]
45. Xiao, Y.; Wang, R.C.; Lu, X.C.; Gao, J.F.; Xu, S.J. Experimental study on the low-temperature dissolution of microperthite in alkaline solution. *Acta Mineral. Sin.* **2003**, *23*, 333–340.
46. Spinthaki, A.; Kamaratou, M.; Disci, D.; Hater, W.; Demadis, K.D. Inhibition of aluminum silicate scaling by phosphonate additives under geothermal stresses. *Geothermics* **2023**, *111*, 102690. [CrossRef]
47. Luo, J.; Zhu, Y.Q.; Guo, Q.H.; Tan, L.; Zhuang, Y.Q.; Liu, M.L.; Zhang, C.H.; Zhu, M.C.; Xiang, W. Chemical stimulation on the hydraulic properties of artificially fractured granite for enhanced geothermal system. *Energy* **2018**, *142*, 754–764. [CrossRef]
48. Ran, H.T.; Cao, J.C.; Zhang, H.F. Effect of interlayer on the existing state of interlayer water in hydrobiotite. *Acta Mineral. Sin.* **1999**, *19*, 215–221.
49. Reed, M.G. Formation permeability damage by mica alteration and carbonate dissolution. *J. Pet. Technol.* **1977**, *29*, 1056–1060. [CrossRef]
50. Yang, F.J.; Wang, G.L.; Hu, D.W.; Zhou, H.; Tan, X.F. Influence of water-rock interaction on permeability and heat conductivity of granite under high temperature and pressure conditions. *Geothermics* **2022**, *100*, 102347. [CrossRef]
51. Hellmann, R.; Tisserand, D. Dissolution kinetics as a function of the Gibbs free energy of reaction: An experimental study based on albite feldspar. *Geochim. Cosmochim. Acta* **2006**, *70*, 364–383. [CrossRef]
52. Crundwell, F.K. The Mechanism of dissolution of the feldspars: Part II Dissolution at conditions close to equilibrium. *Hydrometallurgy* **2015**, *151*, 163–171. [CrossRef]
53. Zhang, F.M. Mechanistic Study on the Effect of Aperture and Roughness on Groundwater Flow in Single Fractures. Master's Thesis, Hefei University of Technology, Hefei, China, 2023.

Disclaimer/Publisher's Note: The statements, opinions and data contained in all publications are solely those of the individual author(s) and contributor(s) and not of MDPI and/or the editor(s). MDPI and/or the editor(s) disclaim responsibility for any injury to people or property resulting from any ideas, methods, instructions or products referred to in the content.